ADVANCED MATERIALS
www.advmat.de

A Polymorphic Memtransistor with Tunable Metallic and Semiconducting Channel

Yonas Assefa Eshete, Eunji Hwang, Junhyung Kim, Phuong Lien Nguyen, Woo Jong Yu, Bai Sun Kong, Min Seok Jang, Jaekwang Lee, Suyeon Cho, and Heejun Yang**

Modulating semiconducting channel potential has been used for electrical switching in transistors without biological plasticity operations that are critical for energy-efficient neuromorphic computing. To achieve efficient data processing, alternative transport mechanisms, such as tunneling and thermionic emission, have been introduced with 2D materials. Here, a polymorphic memtransistor based on atomically thin $Mo_{0.91}W_{0.09}Te_2$ is presented, where the lattice and electronic structures of the lateral device channel can be tuned as either metallic (1T′) or semiconducting (2H) phases by electrical gating. The structural and electronic phase change of the channel material, optimized in $Mo_{0.91}W_{0.09}Te_2$, is explored using transport and optical measurements at the device scale. Based on the phase transition, the polymorphic memtransistor demonstrates a high on/off ratio (up to 10^5), low subthreshold swing (down to 80 mV dec^{-1}), and various memristive behaviors, which are distinguished from traditional phase-change memory, transistors, and passive memristors for diverse neuromorphic and in-memory computing.

1. Introduction

Modulating or switching electrical currents is a basic function of transistors, and has been achieved in conventional silicon-based transistors[1] by modulating channel potential, and by junction energy barrier modulation in graphene barristors.[2] Conceptually new devices, such as various tunnel field-effect transistors[3–5] (FETs) and negative capacitance FETs,[6] have been introduced to further scale down transistors for higher energy efficiency and larger integrated device density in the semiconductor industry. However, such emerging transistors cannot properly address data-intensive tasks involving artificial intelligence (AI) and machine learning, and present understanding of the physical phenomena responsible for negative capacitance is still insufficient.[6] In addition, to overcome the limits of the von Neumann architecture with separated memory and processing units, there have been extensive efforts to develop in-memory computing and memristors[7–10] for AI applications, which require faster data processing with lower energy consumption,[11] exceeding current complementary metal–oxide–semiconductor (CMOS) devices.

Exploiting phase change has been a promising approach to develop novel devices for data-intensive tasks. The Mott metal–insulator transition in TaS_2[12] and VO_2[13] and amorphous-to-crystal transition in $Ge_2Sb_2Te_5$ (GST)[14] have long been studied for Mott transistors[15,16] and nonvolatile memory devices. While electronic (e.g., Mott or CDW transition)[17] and lattice (e.g., GST) phase transitions have been reported as new ways to modulate electric current for transistor and memory applications, critical issues with materials, and device operation remain unresolved. For instance, the effects of atomic vacancies[18] (Mott transition) and Joule heating on integrated device operation require a new material system.

Recently, $MoTe_2$-based materials, which have a small energy difference (<35 meV) between their semiconducting (2H) and metallic (1T′) phases, have been extensively studied for phase engineering.[19–22] Phase engineering applications using the unique polymorphism of $MoTe_2$-based materials include catalytic energy devices,[23,24] ohmic homojunction,[25] and memristors.[26] We note that the phase transition between the 2H and 1T′ phases in $MoTe_2$-based materials clearly contrasts with

Y. A. Eshete
Department of Energy Science
Sungkyunkwan University
Suwon 16419, South Korea

E. Hwang, H. Yang
Department of Physics
Korea Advanced Institute of Science and Technology (KAIST)
Daejeon 34141, South Korea
E-mail: h.yang@kaist.ac.kr

J. Kim, M. S. Jang
School of Electrical Engineering
Korea Advanced Institute of Science and Technology (KAIST)
Daejeon 34141, South Korea

P. L. Nguyen, J. Lee
Department of Physics
Pusan National University
Busan 46241, South Korea

W. J. Yu, B. S. Kong
Department of Electrical and Computer Engineering
Sungkyunkwan University
Suwon 16419, South Korea

S. Cho
Division of Chemical Engineering and Materials Science
Graduate Program in System Health Science and Engineering
Ewha Womans University
Seoul 03760, South Korea
E-mail: s.cho@ewha.ac.kr

The ORCID identification number(s) for the author(s) of this article can be found under https://doi.org/10.1002/adma.202209089.

DOI: 10.1002/adma.202209089

 © 2023 Wiley-VCH GmbH

former phase-change-based devices, such as Mott transistors or GST-based memory devices, in terms of single-crystalline lattice control and operating energy. Although gate-tunable phase change has been observed in $MoTe_2$ by optical methods,[27] actual device operation via polymorphic control requires a more uniform and reliable phase change in the channel at device scale at room temperature, which has not been demonstrated yet. Moreover, the contact resistance deters the transistor switching operation in the phase-engineered device, which should be resolved without complicated fabrication steps.

In this study, we report on a polymorphic memtransistor based on an atomically thin material, $Mo_{0.91}W_{0.09}Te_2$. The stoichiometric ratio of molybdenum and tungsten elements has been optimized in the alloy material to facilitate the electrical phase control of the material. Thus, the hexagonal (2H, semiconducting) and monoclinic (1T′, metallic) structures of $Mo_{0.91}W_{0.09}Te_2$ can be controlled with memristive behaviors (i.e., hysteresis in transport) by the charge carrier density modulated by electrical gating. The phase change occurs at device scale, which is supported by Raman spectroscopy (lattice structure changes) and transport measurements (electronic structure changes). Our polymorphic memtransistor exhibits a high on/off current ratio (up to 10^5) with a subthreshold swing down to 80 mV dec^{-1} and memristive behaviors. As a conceptual device, our memristor demonstrates novel operation mechanism and will pave the way for further investigation of the device parameters and specifications for possible diverse neuromorphic applications including reservoir computing and in-memory computing.[9,10] The direct switching between single-crystalline lattice structures (polymorphs) and the resulting current modulation with memristive behaviors in the device channel contrast sharply with other traditional phase-change memory devices, transistors, and passive memristors.[28]

2. Optimizing Phase-Change Materials Based on $Mo_{1-x}W_xTe_2$

A series of $Mo_{1-x}W_xTe_2$ crystals were synthesized using the chemical vapor transport (CVT) method.[19] The structural phase transition between the hexagonal (2H) and monoclinic (1T′) phases in $Mo_{1-x}W_xTe_2$ was investigated as a function of their atomic ratio of tungsten (x) by X-ray diffraction (XRD), Raman spectroscopy (Figure S2, Supporting Information), and X-ray absorption spectroscopy (XAS) (Figure S3, Supporting Information). The details of the synthesis method and characterizations of $Mo_{1-x}W_xTe_2$ are described in the Supporting information. The critical atomic ratio of tungsten elements in the alloy series for the phase transition between the 2H and 1T′ phases was found to be $x = 0.1$, which is consistent with the reported value.[29] The Raman and XAS spectra of $Mo_{1-x}W_xTe_2$ samples demonstrate a sharp transition between the 2H and 1T′ phases at $x = 0.1$, without mixed phases of 2H and 1T′. A schematic of the operating mechanism of our polymorphic $Mo_{0.91}W_{0.09}Te_2$-based memtransistor is shown in **Figure 1**a.

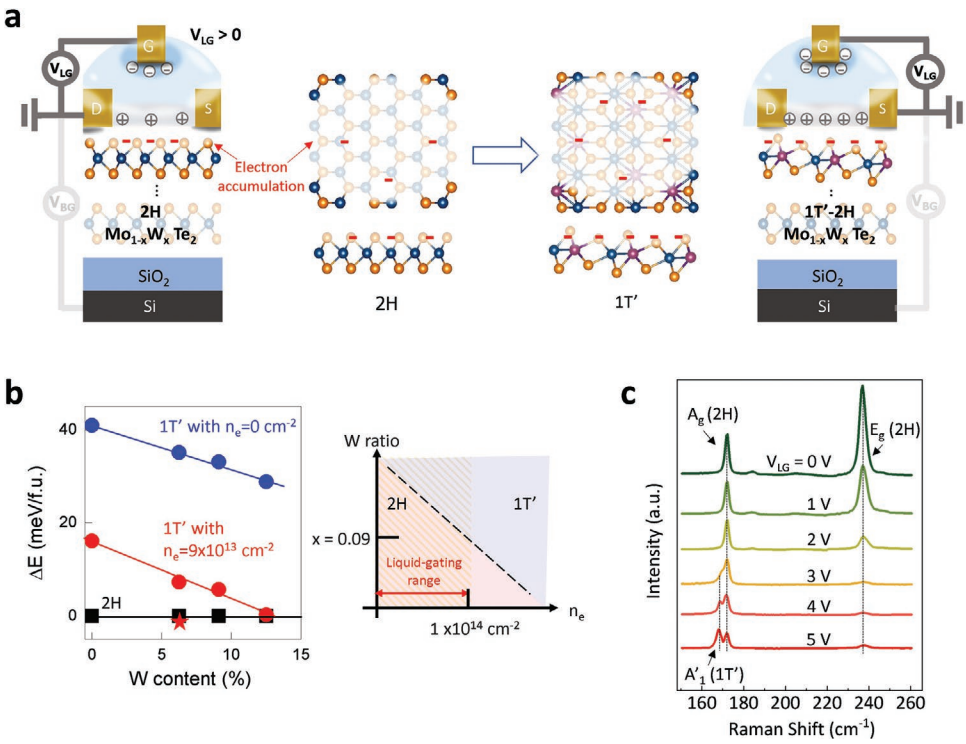

Figure 1. Electrical gating-induced phase transition in $Mo_{0.9}W_{0.1}Te_2$. a) A schematic of the phase transition by liquid ionic gating in $Mo_{0.91}W_{0.09}Te_2$. The semiconducting 2H and metallic 1T′ phases can be switched by V_{LG}. b) The energy difference (ΔE) between the 2H (set as 0 meV/f.u. with various tungsten ratios and electron densities) and 1T′ phases was obtained by first-principles calculations as a function of tungsten atomic ratio (x) and electron density (n_e) (left). The red asterisk indicates $\Delta E = 0$ meV/f.u. with $n_e = 1.0 \times 10^{14}$ cm^{-2} (left). A phase diagram based on the phase stability of the 2H and 1T′ phase with x and n_e (right). c) The gate-dependent in situ Raman spectra taken from bilayer $Mo_{0.91}W_{0.09}Te_2$. The A_g and E_g Raman modes originate from the 2H phase and the A'_1 Raman mode comes from the 1T′ phase.

© 2023 Wiley-VCH GmbH

15214095, 2023, 15, Downloaded from https://onlinelibrary.wiley.com/doi/10.1002/adma.202209089 by Korea Advanced Institute Of, Wiley Online Library on [30/04/2023]. See the Terms and Conditions (https://onlinelibrary.wiley.com/terms-and-conditions) on Wiley Online Library for rules of use; OA articles are governed by the applicable Creative Commons License

The feasibility of electrical manipulation of the 2H and 1T′ phases was investigated by first-principles calculations. The energy difference between the two phases is plotted with various tungsten ratios (x) and electron densities in Figure 1b. Based on the theoretical results, we designed a polymorphic transistor using few-layered $Mo_{1-x}W_xTe_2$ with a critical atomic ratio of tungsten ($x = 0.09$, and thus $Mo_{0.91}W_{0.09}Te_2$), where the energy difference between the 2H and 1T′ phases becomes negligible with a reasonable carrier concentration by electrical gating (i.e., marked by the red asterisk with $n_e = 1 \times 10^{14}$ cm^{-2} in Figure 1b). The negligible energy difference enables a gate-driven phase transition, which is hard to demonstrate with pristine 2H-$MoTe_2$ (indicated by blue circles in Figure 1b), which has an energy difference of 35 meV between the two phases.[20]

3. Gate-Driven Phase Transition in $Mo_{0.91}W_{0.09}Te_2$

We adopted the electric double layer transistor (EDLT) geometry based on the ionic liquid gating method[27]; more details about the EDLT device fabrication and measurements are shown in the Supporting Information. Considering that an electric gating field is effectively screened within a distance of 1 nm-scale[30] in the EDLT geometry, the phase transition in $Mo_{0.91}W_{0.09}Te_2$ might not completely occur in the entire vertical region. The top atomic layer of a $Mo_{0.91}W_{0.09}Te_2$ memtransistor can be most effectively controlled between semiconducting 2H and metallic 1T′ phase by electrical gating, as shown in Figure 1a.

To estimate the accumulated charge density by the liquid ionic gating, we conducted separate Hall measurements (Figure S5, Supporting Information). Using the charge density results from the Hall measurements, the capacitance of the ionic liquid gating (C_{IL}) was found to be 8.5×10^{-6} F cm^{-2}, which is 1000 times higher than that of conventional solid dielectric materials such as SiO_2 and h-BN. Accordingly, the carrier density in the $Mo_{0.91}W_{0.09}Te_2$ (2H phase) device channel reaches 2×10^{14} cm^{-2} with the ionic gating method, which is larger than the expected critical carrier concentration for phase transition (Figure 1b).

To confirm the structural phase transition during electrical gating, we conducted in situ Raman spectroscopy of a bilayer $Mo_{0.91}W_{0.09}Te_2$-based memtransistor by varying the liquid gate bias (V_{LG}). Characteristic Raman modes of the 2H phase without gate bias ($V_{LG} = 0$) are shown in Figure 1c; the A_g and E_g modes were observed at 171.5 and 236 cm^{-1}, respectively. As V_{LG} increases, the relative intensities between the A_g and E_g modes abruptly changes at a critical V_{LG}, while their peak positions and widths remain the same. At a V_{LG} of 3 V, the A'_1 mode, coming from the 1T′ phase, newly appears at 167.5 cm^{-1}. As V_{LG} increases up to 5 V, the intensity of the A'_1 mode increases while the intensity of the A_g and E_g modes decrease without notable changes in peak position or width.

Considering that the ionic gating is more effective for the top atomic layer, the in situ Raman results in Figure 1c show that the top layer of the bilayer $Mo_{0.91}W_{0.09}Te_2$ channel is mostly converted to the 1T′ phase (from the 2H phase) by the electrical gating-driven electrons with a sufficient electron density. The bottom layer of the channel still partly remains in the 2H phase, not showing particular shifts or broadening of Raman modes (A_g and E_g peaks). We interpret the superposed Raman spectra to indicate the formation of a clean heterophase interface (the bottom atomic layer in 2H phase and the top atomic layer in 1T′ phase) in the bilayer $Mo_{0.91}W_{0.09}Te_2$.

The A_g and E_g modes (coming from 2H phase) are clearly observed up to a gate bias of 5 V. However, the Raman peaks become weak at large gate bias (>6 V), probably due to the quenching effect of Raman signals originated from Pauli blocking[31] (Figure S6, Supporting Information). We note that the gating-induced phase transition between 2H and 1T′ in the $Mo_{0.91}W_{0.09}Te_2$ memtransistor is reversible, and the Raman modes show consistent and reliable features with increasing and decreasing gate bias (Figure S7, Supporting Information).

4. Polymorphic Memtransistor Based on Phase Transition of Channel Material

In addition to probing the optical and structural features of the phase transition by in situ Raman spectroscopy, the device-scale control of the electric resistance (or conductance) of our polymorphic memtransistor is critical for practical applications of the phase transition. Thus, we demonstrated reversible resistance control by a gating-induced phase transition between the metallic (1T′) and semiconducting (2H) states, as shown in **Figure 2**.

The four-terminal device geometry, adopted to avoid the contact resistance effect, is shown in Figure 2a. It was possible to investigate the pristine nature of the phase transition by excluding the contact effect in the four-terminal device geometry. Two and three layers of $Mo_{0.91}W_{0.09}Te_2$ were used to fabricate D1 and D2 devices (Figure 2a) to study the thickness-dependent transport features of the revisable phase transition by sweeping V_{LG}. The blue arrows in the transfer curves (the right panel in Figure 2a) indicate there was a sharp drop in resistance in the D1 and D2 devices, originating from the first order structural phase transition from the 2H to 1T′ phase around a critical transition voltage of 4.1 V. The two devices (D1 and D2) exhibited slightly different values of critical V_{LG} for the phase transition (the blue arrows in the inset in Figure 2a) in the transfer curves.

The phase transition-induced resistance change can be clearly distinguished from the electric gating effect in the ambipolar semiconductor ($Mo_{0.91}W_{0.09}Te_2$), as shown in Figure 2b. Different sweep ranges of V_{LG} were used for the D1 device to separately show the two effects in Figure 2b; the ambipolar electrostatic gating effect in the $Mo_{0.91}W_{0.09}Te_2$ device appears around $V_{LG} = 0$ V, and the structural phase transition occurs around $V_{LG} = 4$ V in the D1 device. It was observed that the phase transition (with V_{LG} above 4 V) accompanies hysteresis in the transfer curves, which illustrates the operation of our polymorphic memtransistor. The origin of the hysteresis is not from charge traps formed by sweeping V_{LG} because our in situ Raman spectroscopy in Figure 1c clearly shows the signature of the phase transition between the 2H and 1T′ states with the same V_{LG}.

© 2023 Wiley-VCH GmbH

15214095, 2023, 15, Downloaded from https://onlinelibrary.wiley.com/doi/10.1002/adma.202209089 by Korea Advanced Institute Of, Wiley Online Library on [30/04/2023]. See the Terms and Conditions (https://onlinelibrary.wiley.com/terms-and-conditions) on Wiley Online Library for rules of use; OA articles are governed by the applicable Creative Commons License

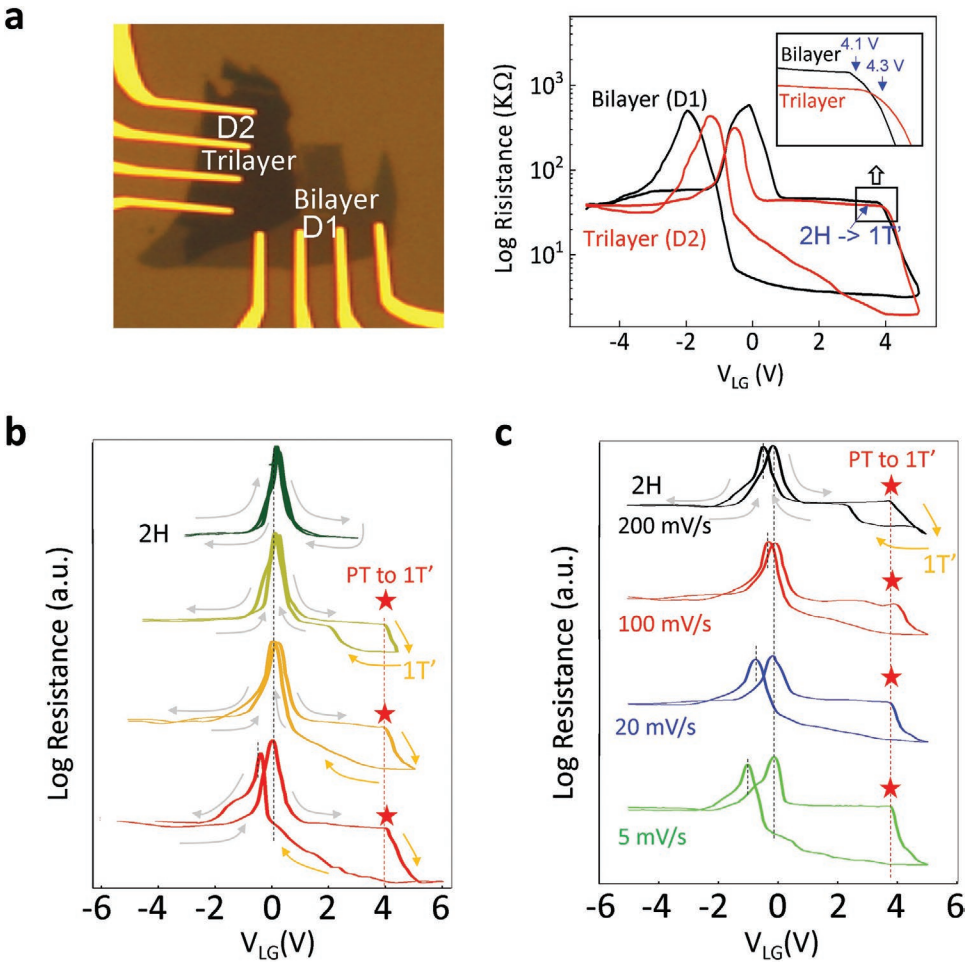

Figure 2. Phase transition in $Mo_{0.91}W_{0.09}Te_2$ devices. a) Optical microscopy image of four-terminal devices D1 and D2 fabricated with bilayer and trilayer $Mo_{0.9}W_{0.1}Te_2$, respectively. The transfer curve of D1 (by liquid gating, V_{LG}) is shown in the right panel. b) Transfer curves with various V_{LG} ranges. The colored arrows indicate the V_{LG} sweep directions with different phases: grey and yellow arrows for the 2H and 1T′ phases, respectively. The red asterisks show the critical V_{LG} for the 2H to 1T′ phase transition (PT). c) Transfer curves with various sweep rates of V_{LG}.

The transport results in Figures 2 and Figure S8, Supporting Information, are consistent with the calculated energy differences in Figure 1b; metallic 1T′ becomes more stable than the semiconducting 2H phase at an electron density of 2.1×10^{14} cm^{-2} with a tungsten atomic ratio of $x = 0.09$. Strong hole doping could not induce the reversible phase transition between the 2H and 1T′ phases in our study, and this is also consistent with the theoretical study (Figure 1b). We limited the range of V_{LG} (absolute values) to 6 V because a higher V_{LG} could induce unwanted electrochemical reactions in the device channel in our study. The gate leakage current exceeded a few nanoamperes with a V_{LG} larger than 6 V, suggesting that there could be electrochemical effects with a large V_{LG}, as shown in Figure S8, Supporting Information.

Transfer curves with various scan speeds of V_{LG} are shown in Figure 2c. The capacitive charging effect in the ionic liquid gating enables lower resistance states and larger hysteresis curves with a slower scan speed of V_{LG} (e.g., the green curve in Figure 2c). We note that a slow sweep of 5 mV s^{-1} maintained the 1T′ phase at $V_{LG} = 0$ V, which exhibited nonvolatile memtransistor behavior with a large hysteresis window.

The shift in the charge neutrality point (maximum resistance peak) toward negative V_{LG} (in the decreasing V_{LG} direction) in Figure 2b,c originates from charge traps and the resulting doping effect that occurs with high V_{LG}. To exclude the doping effect in our polymorphic memtransistor operation, we used a V_{LG} range from −5 to 5 V and a scan rate of 20 mV s^{-1} in the following measurements.

The reliability and stability of the structural phase transition at device scale are demonstrated by the cyclic transfer curves of the D1 device, as shown in Figure S9, Supporting Information. We measured the transfer curves of the D1 device with a scan rate of 20 mV s^{-1} for 7 h in Figure S9, Supporting Information. The phase transition is reliable over the cyclic measurements, and the critical V_{LG} for phase transition gradually decreases from 4.1 to 3.3 V, shown in the first derivative resistance plot in Figure S9, Supporting Information. We explain the shift in critical V_{LG} by the generation of Te vacancies during the liquid ionic gating, which induces electron doping.[32] Moreover, we can use a certain condition of liquid ionic gating to electrochemically etch the device channel (Figure S15, Supporting Information), further decreasing the critical V_{LG} for phase transition.

© 2023 Wiley-VCH GmbH

15214095, 2023, 15, Downloaded from https://onlinelibrary.wiley.com/doi/10.1002/adma.202209089 by Korea Advanced Institute Of, Wiley Online Library on [30/04/2023]. See the Terms and Conditions (https://onlinelibrary.wiley.com/terms-and-conditions) on Wiley Online Library for rules of use; OA articles are governed by the applicable Creative Commons License

5. Improving Contact Resistance for Two-Terminal Memory and Synaptic Devices

Reducing contact resistance has been a long-standing issue in semiconductor devices. In the four-terminal device geometry in Figure 2a, the contacts (or junctions) between the metallic electrodes and the semiconducting channel are protected from the liquid ionic gating. The effect of large contact resistance was excluded by using the four-terminal device in Figure 2. Nevertheless, we note that practical semiconductor device applications require low contact resistance to enable two-terminal field-effect device operation. Phase engineering has been used to reduce contact resistance by forming homojunctions with laser patterning.[25]

It is known that a "forming process" is required for oxide-based nonvolatile memory devices (e.g., resistive random access memory, RRAM). In this study, we demonstrate a forming process by sweeping V_{LG}, which achieves optimized contacts in our polymorphic memtransistor without extra fabrication steps such as laser patterning. The progressive phase evolution of $Mo_{0.91}W_{0.09}Te_2$ underneath metal electrodes is shown in **Figure 3**a. The contact phase engineering is based on the proximity effect of the liquid gating; the 1T′ phase of $Mo_{0.91}W_{0.09}Te_2$ is first formed in the channel area, and induces a further phase transition under the metal electrodes by proximity electron doping effects during the V_{LG} sweep.

The reduced contact resistance between the metal electrodes and the channel enables the polymorphic memtransistor to operate in the two-terminal geometry, as shown in the transfer curves in Figure 3b. The red asterisks in the middle and right panels in Figure 3b exhibit the abrupt current (or resistance) change produced by the phase transition, not excluding the contact resistance (in the two-terminal measurement).

Before the forming process, no phase transition is observed with V_{LG} sweep in the two-terminal geometry, as shown in the left panel in Figure 3b. Once the forming process is conducted, the phase transition is observed in the two-terminal geometry (middle and right panels in Figure 3b), which is similar to the

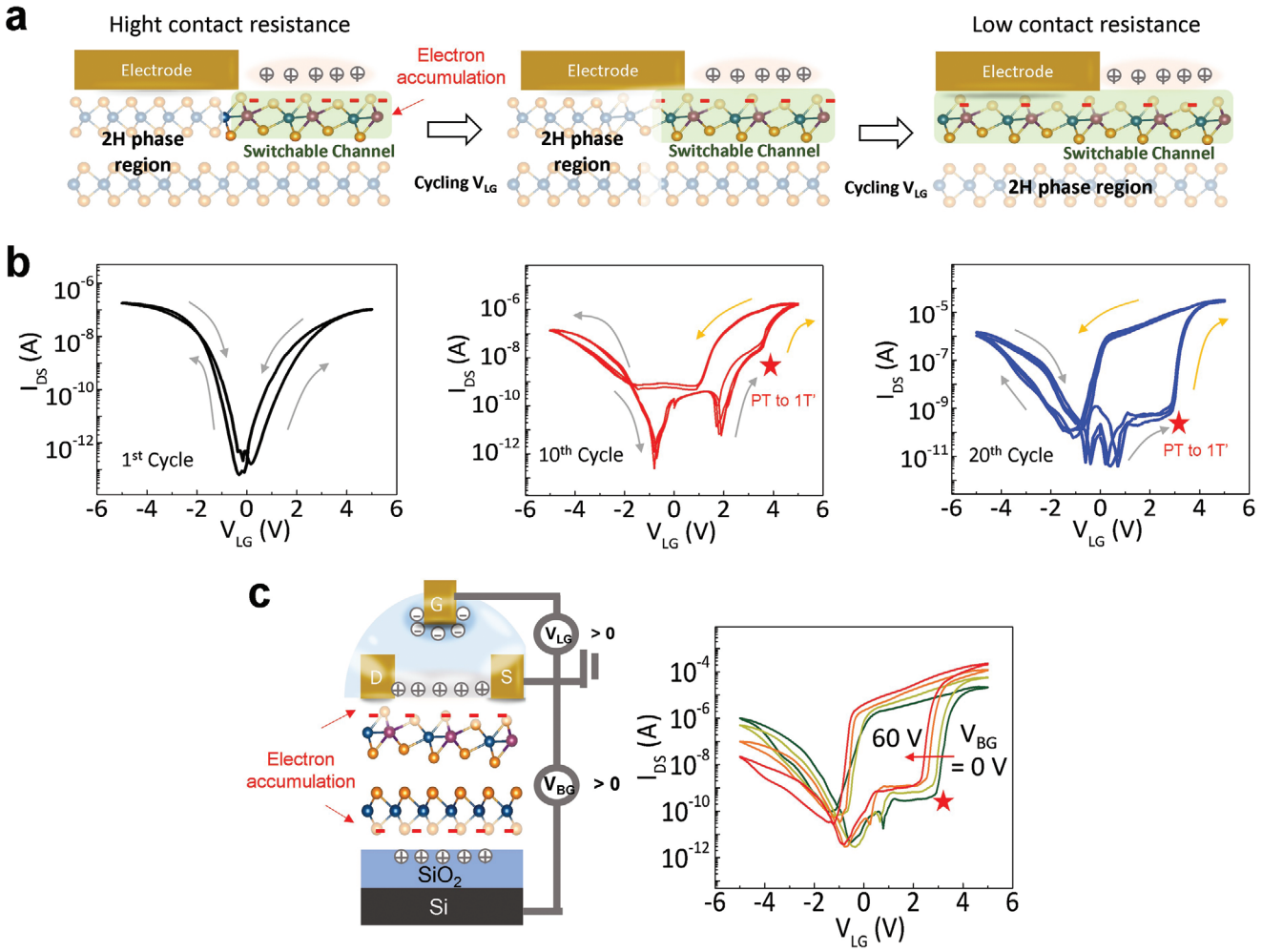

Figure 3. Phase-driven contact engineering. a) The forming process of the $Mo_{0.91}W_{0.09}Te_2$-based memtransistor. During the forming process, a phase change from the 2H to the 1T′ phase progressively occurs underneath the electrode, which produces a low contact resistance. b) Three transfer curves by V_{LG}. The typical ambipolar transfer curve is observed without any phase transition before the forming process (the black curve in the left panel). As the forming process continues, an abrupt increase in current takes place in positive V_{LG}, with electron accumulation (the red (middle) and blue (right) transfer curves). c) Dual-gate measurements that show further decrease in the critical V_{LG} for phase transition.

© 2023 Wiley-VCH GmbH

15214095, 2023, 15, Downloaded from https://onlinelibrary.wiley.com/doi/10.1002/adma.202209089 by Korea Advanced Institute Of, Wiley Online Library on [30/04/2023]. See the Terms and Conditions (https://onlinelibrary.wiley.com/terms-and-conditions) on Wiley Online Library for rules of use; OA articles are governed by the applicable Creative Commons License

result obtained with four-terminal measurements in Figure 2. The current switching via the phase transition shows a stable and large window of hysteresis with a promising value of subthreshold swing of 80 mV dec^{-1} in the two-terminal device operation.

The critical V_{LG} for phase transition can be further controlled by dual-gating, as shown in Figure 3c. The back-gating through SiO_2 (V_{BG}) facilitates the gate-driven phase transition. The critical V_{LG} reaches 2.6 V with a V_{BG} of 60 V. Negative V_{BG} induces additional hole carriers in $Mo_{0.91}W_{0.09}Te_2$, which makes it harder for the phase transition and hysteresis in the transfer curves (i.e., memtransistor characteristics), shown in Figure S11, Supporting Information.

6. Conclusion

The current von Neumann architecture based on conventional semiconducting devices cannot properly address data-intensive tasks involving AI, machine learning, and Internet of Things (IoT) in the future. While emulating biological, complex neural networks is considered a promising solution for those future technologies, optimized materials for energy-efficient, and biological plasticity operations are still lacking.

We conceived a polymorphic memtransistor based on $Mo_{0.91}W_{0.09}Te_2$. The small energy difference between the semiconducting 2H and metallic 1T′ phases in the optimized polymorphic material provides a unique opportunity to develop a conceptually new and energy-efficient polymorphic memtransistor. The nontrivial electric switching of current with memristive characteristics distinguishes this approach from traditional phase-change memory, transistors and passive memristors, and is promising for diverse neuromorphic and in-memory computing.

7. Experimental Section

Synthesizing $Mo_{1-x}W_xTe_2$ for Phase Transition: $Mo_{1-x}W_xTe_2$ single crystals were grown using the CVT method. 99.95% pure Mo (Sigma Aldrich), 99.98% pure W (Sigma Aldrich) powder, and 99.95% pure Te (Sigma Aldrich) pellets were used with precise stoichiometric ratio; the mixed powders were ground and sealed in a vacuum quartz tube and iodine powders (3 mg; 99.99% purity) (Sigma Aldrich) were put together. The quartz tube was put at the center of a two-zone CVT furnace and a temperature gradient was applied by 100 °C (1150 °C at one end and the other end was maintained at a temperature of 1050 °C) for two weeks. To obtain gray and shiny crystals of the 2H and 1T′ phases of $Mo_{1-x}W_xTe_2$, the temperature was slowly cooled to room temperature. In particular, the authors focused $x = 0.09$ for the most subtle stoichiometric ratio for phase transition.

The characterization of the elemental distribution and chemical composition of an exfoliated thin film of $Mo_{1-x}W_xTe_2$ alloy was conducted via JSM-7900F Schottky FE-SEM elemental mapping and EDS analysis (Figure S1, Supporting Information). The $Mo_{1-x}W_xTe_2$ alloy demonstrated uniform spatial distribution of the constituent elements and near actual nominal composition. The sharp structural phase transition from the 2H to the 1T′ phase was observed via several structural characterization techniques. X-ray diffraction (XRD) measurements were conducted on the single crystal samples using an X-ray diffractometer (Rigaku, Smart Lab). An X-ray Generator, 9 kW and 2θ scanned from 10° to 70° (angle) were used to collect XRD data. The phonon properties (Raman spectroscopy) of the sample were studied by confocal Raman spectroscopy (NT-MDT, NTEGRA) using a 531 and 633 nm laser as an optical source. Composition dependent XAS was measured on the 1C beamline of the Pohang Light Source, Korea, in the fluorescence yield mode.

Electric Double Layer Transistor (EDLT)-Device Fabrication: A few layers of $Mo_{0.91}W_{0.09}Te_2$ flake were exfoliated to fabricate various device geometries, with an isolated side electrode to control the liquid gate voltage, V_{LG}. Thin flakes of $Mo_{0.91}W_{0.09}Te_2$ with the proper thickness (2–4 layers) were roughly identified by analyzing the thickness dependent Raman intensity.[33] Atomically flat, high-quality $Mo_{0.91}W_{0.09}Te_2$ flakes were subsequently selected for further fabrication procedures.

Once the flake was isolated, standard electron beam lithography (EBL) was used to pattern various geometry devices, hall bar structure, four-terminal and two-terminal geometry and then developed by methyl isobutyl ketone (MIBK) solution. The developed pattern was deposited with Cr/Au (5/50 nm) contact electrodes, since Cr provides good adhesion and electrical contacts with the sample. Hot Acetone (60 °C) was used for the lift-off process. Additional standard electron beam lithography (EBL) was performed to selectively expose (open window) only the device channel and gate pad area to the ion gale while all remaining device parts were passivated with PMMA-C7 photoresist, as shown in Figure S4, Supporting Information. This type of device passivation enables the ions to be focused in the device channel for maximum gating efficacy, and also suppresses unnecessary side electrochemical reactions.

A 25 mL ionic liquid: *N*,*N*-diethyl-*N*-(2-methoxyethyl)-*N*-methylammonium bis-(trifluoromethylsulfonyl)-imide (DEME-TFSI) was carefully dropped onto the center of the device connecting the device channel and gate pad, inside an Ar-filled glove box. The device was annealed at high vacuum (10^{-6} Torr) for over 12 h before measurement, to remove any moisture absorbed by the ionic liquid, and to enable a high performance device.

Device Measurements and Analysis: All liquid gating based optical and device measurements were performed at low temperature, 220 K and high vacuum, up to 1×10^{-7} Torr. The performance of ionic liquids was very sensitive to the presence of moisture and electrochemical reactions at high temperature, which deters the reversible and reliable operation of the devices. The typical device measurement was performed at a gate scan rate of 20 mV s^{-1}, which provided optimum time for ionic movement, to avoid histolysis while minimizing total exposure time of the device to the ionic liquid and reduced electrochemical contribution. Despite the small hysteresis observed due to the slow motion of ions, the device measurement was reversible and reproducible.

The four-terminal and Hall resistance were measured by applying a current level of 1 μA between the source and drain electrodes and collecting the longitudinal voltage drops (V_{xx}) and transverse voltages drops (V_{xy}), respectively. All transport measurements of the device were executed using a Lakeshore low temperature hall measurement system with cryogenic probe station (chamber pressure = 5×10^{-5} to 10^{-7} Torr) cooled with a closed-circuit refrigerator (CCR) loop of liquid helium and connected to a Keithley 4200-SCS parameter analyzer.

Supporting Information

Supporting Information is available from the Wiley Online Library or from the author.

Acknowledgements

This research was supported by the Samsung Research Funding & Incubation Center of Samsung Electronics, under project no. SRFC-MA1701-01 and by National Research Foundation of Korea (NRF) under Grant No. NRF-2021M3H4A1A03054856. S.C. was supported by the Basic Science Research Program through the National Research

© 2023 Wiley-VCH GmbH

15214095, 2023, 15, Downloaded from https://onlinelibrary.wiley.com/doi/10.1002/adma.202209089 by Korea Advanced Institute Of, Wiley Online Library on [30/04/2023]. See the Terms and Conditions (https://onlinelibrary.wiley.com/terms-and-conditions) on Wiley Online Library for rules of use; OA articles are governed by the applicable Creative Commons License

Foundation of Korea (NRF) funded by the Ministry of Science, ICT and Future Planning (MSIT) (2020K1A3A7A09080370). J. K. and M. S. J. acknowledge the support by the NRF grant funded by MSIT (2022R1A2C2092095). KAIST-funded Global Singularity Research Program for 2021 (HY).

Conflict of Interest

The authors declare no conflict of interest.

Author Contributions

Y.A.E., E. H., S.C., and H.Y. conceived the idea and designed the project. Y.A.E. grew the single crystals and performed the basic characterizations. J.K. and M.S.J. conducted Raman measurements. W.J.Y. and B.S.K. analyzed memristive behaviors. P.L.N. and J. L. conducted theoretical simulations. Y.A.E., S.C., and H.Y. wrote the manuscript with input from all the authors.

Data Availability Statement

The data that support the findings of this study are available from the corresponding author upon reasonable request.

Keywords

alloys, in-memory computing, memtransistors, phase transitions, polymorphism

Received: October 2, 2022
Revised: January 15, 2023
Published online: March 3, 2023

[1] L. Mark, *Science* **2003**, *299*, 210.
[2] H. Yang, J. Heo, S. Park, H. J. Song, D. H. Seo, K.-E. Byun, P. Kim, I. Yoo, H.-J. Chung, K. Kim, *Science* **2012**, *336*, 1140.
[3] M E. Beck, A. Shylendra, V. K. Sangwan, S. Guo, W. A. Gaviria Rojas, H. Yoo, H. Bergeron, K. Su, A. R. Trivedi, M. C. Hersam, *Nat. Commun.* **2020**, *11*, 1565.
[4] D. Sarkar, X. Xie, W. Liu, W. Cao, J. Kang, Y. Gong, S. Kraemer, P. M. Ajayan, K. Banerjee, *Nature* **2015**, *526*, 91.
[5] E. Kim, G. Hwang, D. Kim, D. Won, Y. Joo, S. Zheng, K. Watanabe, T. Taniguchi, P. Moon, D.-W. Kim, L. Sun, H. Yang, *Adv. Mater.* **2022**, *34*, 2106625.
[6] W. Cao, K. Banerjee, *Nat. Commun.* **2020**, *11*, 196.
[7] L. Sun, Z. Wang, J. Jiang, Y. Kim, B. Joo, S. Zheng, S. Lee, W. J. Yu, B.-S. Kong, H. Yang, *Sci. Adv.* **2021**, *7*, eabg1455.
[8] L. Sun, Y. Zhang, G. Han, G. Hwang, J. Jiang, B. Joo, K. Watanabe, T. Taniguchi, Y.-M. Kim, W. J. Yu, B.-S. Kong, R. Zhao, H. Yang, *Nat. Commun.* **2019**, *10*, 3161.
[9] D. Ielmini, H.-S. P. Wong, *Nat. Electron.* **2018**, *1*, 333.
[10] A. Sebastian, M. Le Gallo, R. Khaddam-Aljameh, E. Eleftheriou, *Nat. Nanotechnol.* **2020**, *15*, 529.
[11] F. Zhou, Z. Zhou, J. Chen, T. H. Choy, J. Wang, N. Zhang, Z. Lin, S. Yu, J. Kang, H.-S. P. Wong, Y. Chai, *Nat. Nanotechnol.* **2019**, *14*, 776.
[12] D. Kim, E.-C. Shin, Y. Lee, Y. H. Lee, M. Zhao, Y.-H. Kim, H. Yang, *Nat. Commun.* **2022**, *13*, 4516.
[13] You Zhou, S. Ramanathan, *Proc. IEEE* **2015**, *103*, 1289.
[14] H.-S. P. Wong, S. Raoux, S. Kim, J. Liang, J. P. Reifenberg, B. Rajendran, M. Asheghi, K. E. Goodson, *Proc. IEEE* **2010**, *98*, 2201.
[15] I H. Inoue, M. J. Rozenberg, *Adv. Funct. Mater.* **2008**, *18*, 2289.
[16] M. Nakano, K. Shibuya, D. Okuyama, T. Hatano, S. Ono, M. Kawasaki, Y. Iwasa, Y. Tokura, *Nature* **2012**, *487*, 459.
[17] D. Won, D. H. Kiem, H. Cho, D. Kim, Y. Kim, M. Y. Jeong, C. Seo, J. Kim, J.-G. Park, M. J. Han, H. Yang, S. Cho, *Adv. Mater.* **2020**, *32*, 1906578.
[18] J. Jeong, N. Aetukuri, T. Graf, T. D. Schladt, M. G. Samant, S. S. P. Parkin, *Science* **2013**, *339*, 1402.
[19] D. H. Keum, S. Cho, J. H. Kim, D.-H. Choe, Ha-J Sung, M. Kan, H. Kang, J.-Y. Hwang, S. W. Kim, H. Yang, K. J. Chang, Y. H. Lee, *Nat. Phys.* **2015**, *11*, 482.
[20] Y. Li, K-A. N. Duerloo, K. Wauson, E. J. Reed, *Nat. Commun.* **2016**, *7*, 10671.
[21] H. Yang, S. W. Kim, M. Chhowalla, Y. H. Lee, *Nat. Phys.* **2017**, *13*, 931.
[22] Y. A. Eshete, K. Kang, S. Kang, Y. Kim, P. L. Nguyen, D. Y. Cho, Y. Kim, J. Lee, S. Cho, H. Yang, *Adv. Mater.* **2022**, *34*, 2202633.
[23] Y. Lee, N. Ling, D. Kim, M. Zhao, Y. A. Eshete, E. Kim, S. Cho, H. Yang, *Adv. Funct. Mater.* **2022**, *32*, 2105675.
[24] Y. A. Eshete, N. Ling, S. Kim, D. Kim, G. Hwang, S. Cho, H. Yang, *Adv. Funct. Mater.* **2019**, *29*, 1904504.
[25] S. Cho, S. Kim, J. H. Kim, J. Zhao, J. Seok, D. H. Keum, J. Baik, D.-H. Choe, K. J. Chang, K. Suenaga, S. W. Kim, Y. H. Lee, H. Yang, *Science* **2015**, *349*, 625.
[26] F. Zhang, H. Zhang, S. Krylyuk, C. A. Milligan, Y. Zhu, D. Y. Zemlyanov, L. A. Bendersky, B. P. Burton, A. V. Davydov, J. Appenzeller, *Nat. Mater.* **2019**, *18*, 55.
[27] Y. Wang, J. Xiao, H. Zhu, Y. Li, Y. Alsaid, K. Y. Fong, Y. Zhou, S. Wang, Wu Shi, Y. Wang, A. Zettl, E. J. Reed, X. Zhang, *Nature* **2017**, *550*, 487.
[28] L. Sun, W. Wang, H. Yang, *Adv. Intell. Syst.* **2020**, *2*, 1900167.
[29] D. Rhodes, D. A. Chenet, B. E. Janicek, C. Nyby, Y. Lin, W. Jin, D. Edelberg, E. Mannebach, N. Finney, A. Antony, T. Schiros, T. Klarr, A. Mazzoni, M. Chin, Y.-C. Chiu, W. Zheng, Q. R. Zhang, F. Ernst, J. I. Dadap, X. Tong, J. Ma, R. Lou, S. Wang, T. Qian, H. Ding, R. M. Osgood, D. W. Paley, A. M. Lindenberg, P. Y. Huang, A. N. Pasupathy, et al., *Nano Lett.* **2017**, *17*, 1616.
[30] J. Ye, M. F. Craciun, M. Koshino, S. Russo, S. Inoue, H. Yuan, H. Shimotani, A. F. Morpurgo, Y. Iwasa, *Proc. Natl. Acad. Sci. USA* **2011**, *108*, 13002.
[31] S. Y. F. Zhao, G. A. Elbaz, D. K. Bediako, C. Yu, D. K. Efetov, Y. Guo, J. Ravichandran, K.-A. Min, S. Hong, T. Taniguchi, K. Watanabe, L. E. Brus, X. Roy, P. Kim, *Nano Lett.* **2018**, *18*, 460.
[32] D. Kim, J. H. Lee, K. Kang, D. Won, M. Kwon, S. Cho, Y.-W. Son, H. Yang, *Adv. Electron. Mater.* **2021**, *7*, 2000823.
[33] C. Ruppert, B. Aslan, T. F. Heinz, *Nano Lett.* **2014**, *14*, 6231.

 © 2023 Wiley-VCH GmbH

15214095, 2023, 15, Downloaded from https://onlinelibrary.wiley.com/doi/10.1002/adma.202209089 by Korea Advanced Institute Of, Wiley Online Library on [30/04/2023]. See the Terms and Conditions (https://onlinelibrary.wiley.com/terms-and-conditions) on Wiley Online Library for rules of use; OA articles are governed by the applicable Creative Commons License